Experimental optical fan beam tomography

Keith E. Bennett, Gregory W. Faris, and Robert L. Byer

Optical tomography is used to map the iodine vapor density in a plane. Two-dimensional images are obtained with 1-cm spatial resolution using a fan beam geometry with a 28-cm radius fan source circle. The images are reconstructed using the convolution backprojection algorithm with data collected in 0.1 sec from 90 detectors on a full circle using 90–360 fan source positions. Experimental results quantitatively confirm a theoretical analysis of the noise in the reconstructed image, including the effects of correlated noise, position within the image, and spatial resolution. The noise amplitude–absorption length product for a 2-cm pixel size is 6×10^{-4} which is equivalent to an iodine concentration of 6 ppm.

I. Introduction

Spatially resolved measurements of the densities of specific species are useful in fluid flow and combustion studies. Computed tomographic reconstructions of absorption measurements provide a 2-D map of specific species density in a planar cross section of a region. This paper describes fan beam optical tomographic imaging of the absorption of a plume of iodine vapor.

The experimental work verifies theoretical predictions of the reconstructed image noise. Specifically, the dependence of the image noise on the distance of the reconstructed point from the center of the fan source circle, the number of fan source positions per revolution, and the correlations of the noise within the projection data are illustrated. In addition, the use of a triangle filter convolved with the reconstruction kernel is shown to effectively reduce the noise in the image.

Computer assisted tomography (CAT scanning) is well established in medical x-ray imaging.[1–5] The measurements for tomographic reconstructions are sets of line integrals of the absorption along a large number of rays crossing the region. There are two geometries commonly used for the ray paths: parallel beam geometry[6] and fan beam geometry.[7] We use fan beam geometry which offers the advantages of rapid data collection and simple implementation. The implementation of a fan beam geometry is greatly simplified by using the virtual source technique described by Byer and Shepp.[8] The images are reconstructed using the convolution backprojection algorithm.

In addition to tomography, several techniques have been demonstrated for spatially resolved species measurements in gases. Mechanical sensors are often unacceptable because they disturb the flow. Although widely used, point probe techniques are relatively slow. Combustion measurements have been made by Dyer and Crosley[9] and Kychakoff *et al.*[10] using the planar laser-induced fluorescence technique. A supersonic jet was investigated by McDaniel *et al.*[11] using off-resonance laser-induced fluorescence. Fluorescence techniques are hampered by quenching which makes the data difficult to interpret quantitatively. A review of quenching with application to quantitative fluorescence measurements has been given by Crosley.[12] Other imaging techniques include Rayleigh and Raman scattering which have been used by Long *et al.*[13] to study a turbulent diffusion flame. Raman techniques suffer from low sensitivity and Rayleigh scattering is not species specific. In contrast to these techniques, absorption tomography remains quantitative even in optically thick systems, does not require access outside the plane of interest, and provides accurate and absolute spatially resolved absorption measurements.

There have been several studies of optical tomography since it was proposed independently by Wolf[14,15] and Berry and Gibbs[16] as an algorithm for the 3-D reconstruction of an optical object from line integrals of the phase or absorption. Optical tomography for remote sensing applications was proposed by Stuck[17] and Byer and Shepp.[8] A model study was performed by Wolfe and Byer.[18] Kirchartz *et al.*[19] used differential interferometry to measure the line integral of the index of refraction and reconstructed the image with an iterative technique. Aerosol distribution has been measured tomographically using light emitting diodes to probe scattering by Willms,[20] who reconstructed the image with an algebraic technique. A parallel beam tomographic imaging system was constructed by San-

The authors are with Stanford University, Applied Physics Department, Stanford, California 94305.

Received 5 November 1983.
0003-6935/84/162678-08$02.00/0.

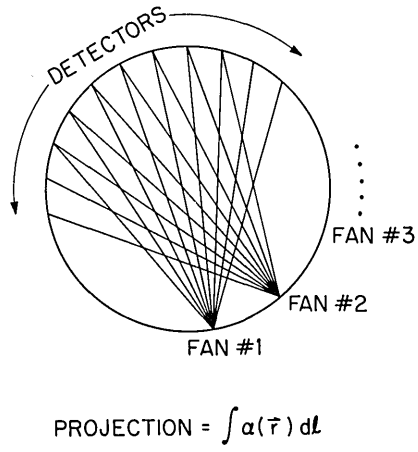

Fig. 1. Fan beam tomography geometry. For each fan source position, the line integral of the absorption along the rays from the source to the detectors is measured. The detectors and fan sources are uniformly spaced along the perimeter of the fan source circle.

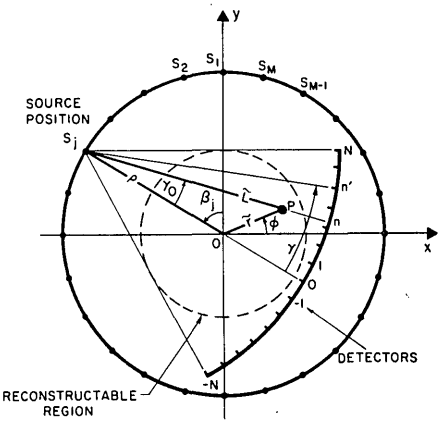

Fig. 2. Fan Beam Geometry. S_j is the jth position of M equally spaced source positions along the perimeter of the fan source circle of radius ρ; β_j is the angle of S_j from the y axis. The $2N + 1$ detectors rotate about the origin O to maintain their positions relative to the source; $\tilde{L}$ is the distance from the source to the reconstructed point $P(x,y)$ with polar coordinates $(\tilde{r},\phi)$; and γ_0 is the angle of the ray in a fan with source at S_j which goes through P. γ is the angle of the ray to detector n'; γ and γ_0 are measured relative to the ray from S_j to O.

toro *et al.*[21] for the investigation of an off-axis methane–air free jet. Santoro utilized the convolution backprojection reconstruction method commonly employed by clinical x-ray computerized tomography scanners. The convolution backprojection algorithm allows for rapid image reconstruction on large grids and is stable with respect to noise in the data.

The convolution backprojection algorithm for tomographic reconstructions is reviewed in Sec. II. Noise is an important consideration in any experimental technique, and our results for the noise in tomographic image reconstructions are summarized in Sec. III. Experimental results demonstrating the imaging capability of tomography and a comparison of the image noise with theoretical predictions are discussed in Sec. IV. Finally, Sec. V is a summary.

II. Convolution Backprojection Reconstruction for Fan Beam Geometry

In fan beam geometry a point source of radiation illuminates a fan of detectors as shown in Fig. 1. In our implementation, the M fan source positions are equally spaced along the perimeter of a circle. The signal at every detector is recorded for each fan position. A total of $(2N + 1)M$ line integrals of the absorption is recorded. It is easily shown that $2N + 1$ detectors which are equally spaced along the perimeter of the fan source circle are also equally spaced in angle as seen from the fan source positions.

The image is reconstructed from the line integrals using the convolution backprojection algorithm for the fan beam geometry derived by Herman and Naparstek.[22] The reconstructed 2-D absorption per unit length, $\mu(\mathbf{r})$, is a convolution of each fan with the kernel k followed by a backprojection sum over all fans given by

$$\mu(\mathbf{r}) = \sum_{j=1}^{M} \frac{\rho}{\tilde{L}^2} \sum_{n'=-N}^{N} k[(n - n')a]h_j(n') \cos(n'a), \qquad (1)$$

where the variables are the geometric quantities shown in Fig. 2. Specifically, ϕ is the polar angle of $\mathbf{r} = (x,y)$ given by $\phi = \arctan(y/x)$, $\mathbf{r}$ is the distance from (x,y) to the center of the fan source circle given by $\tilde{r} = |\mathbf{r}| = (x^2 + y^2)^{1/2}$, $\beta_j = 2\pi j/M$ is the angle of the fan source from the y axis, and ρ is the radius of the fan source circle. $\tilde{L}$ is the distance from the fan source to the point $(\mathbf{r})$ being reconstructed given by $\tilde{L} = \tilde{L}_j = [\rho^2 + \tilde{r}^2 + 2\rho\tilde{r}\sin(\beta_j - \phi)]^{1/2}$, and na is the angle of a ray within the fan to the point $\mathbf{r}$ given by

$$na = \gamma_0 = \arctan\left[\frac{\tilde{r}\cos(\beta_j - \phi)}{\rho + \tilde{r}\sin(\beta_j - \phi)}\right]. \qquad (2)$$

The angle a is the spacing between the rays along which the absorption is measured. The projection data $h_j(n')$ are the integrals of the absorption along the ray at angle $n'a$ from the center line of the fan at angle β_j.

The choice of the kernel function is a compromise between spatial resolution and noise sensitivity. The sampled Ramachandran-Lakshminarayanan (RL)[23] kernel is given by

$$k(na) = \begin{cases} \dfrac{\pi}{4Ma} & n = 0, \\ \dfrac{-a}{\pi M \sin^2(na)} & n = \pm 1, \pm 3 \ldots, \\ 0 & n = \pm 2, \pm 4, \ldots. \end{cases} \qquad (3)$$

The kernel is defined to be linear in the intervals between integer values of n.

The spatial resolution of a tomogram is determined by the kernal used in the convolution. The RL kernel does not include any additional filtering over the Nyquist limit that is mandated by the detector spacing. Hence the angle between detectors and the radius of the fan source circle place an upper bound on the spatial

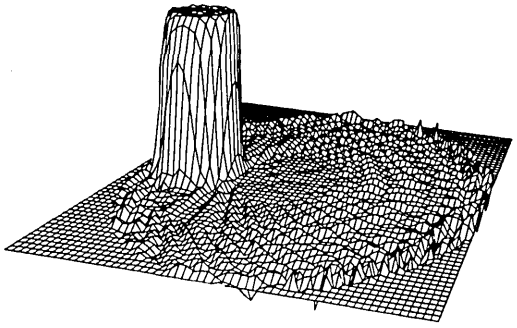

Fig. 3. Fan beam tomography reconstruction showing aliasing from noiseless simulated projections of a disk object. The vertical scale is linear. The reconstructed image is 0.73 of the fan source circle radius using 180 fan source positions with 90 detectors around the full circle.

resolution. Inspection of the convolution backprojection method of reconstruction reveals that the spatial resolution of the RL kernel in the center of the image is approximately one-half of the detector spacing on the fan source circle perimeter. A more detailed discussion of the convolution backprojection reconstruction method and of kernels other than the RL kernel is presented by other authors.[4,24,25]

In addition to statistical noise, which is discussed in the next section, discrete sampling results in insufficient data to exactly reconstruct the object. These reconstruction errors are termed artifacts and fall into two main categories: (1) aliasing and (2) interpolation errors. These occur independently of any statistical noise that may be present.

Aliasing is a problem well known in signal processing and occurs whenever a signal has components at frequencies higher than twice the sampling rate or the Nyquist frequency. The high frequencies show up in the sampled signal at frequencies below the Nyquist frequency. The problem is that the aliased signal is indistinguishable from a true signal at that frequency and generally cannot be removed by filtering after sampling. Aliasing, as it applies to tomography, has been discussed by Brooks *et al.*[26] and Herman.[27] Reconstructions of hard edged objects with the RL filter are almost certain to have aliasing present. Streaks radiating tangentially from the edge of the object are the signature of an aliased tomogram.

Figure 3 shows an example of aliasing. The tomogram was reconstructed from 180 simulated views of a disk object with 90 detectors on a full circle. The radius of the field of the reconstruction is 0.73 of the radius of the fan source circle. Note that the reconstruction is not exact even when the projection data are exact and there is no noise present. Aliasing can be reduced when the number of detector samples per resolvable spot is increased or the source and/or detector are enlarged to attenuate the higher spatial frequencies of the projection data. In other words, there should be several projection rays per resolution element in the reconstruction.

A partial remedy of aliasing, due to Brooks *et al.*,[28] is to look at the object from opposite sides and shift the detectors with respect to the line from the source position through the center of the circle. This effectively halves the sample spacing. Our detectors are fixed, and we did not utilize this option.

The occurrence of star artifacts, the peaks and valleys radiation from the center toward the edge of the reconstruction, is very common. In contrast to the aliasing artifacts described above, these interpolation errors are separated from the object and there is one streak for each fan. Inspection of Fig. 3 reveals that there is a circle within which these streaks are not very significant. Joseph and Schulz[29] have used heuristic arguments to show that the radius R of the artifact-free circle is

$$R = \frac{M\rho}{M + 4\pi\nu_M\rho}, \tag{4}$$

where M is the number of fan positions on a full circle, ρ is the radius of the fan source circle, and ν_M is the maximum spatial frequency which is present. This result shows that the artifact-free radius asymptotically approaches ρ as $M \to \infty$. The number of views required to avoid artifacts at radius R from objects with spatial frequencies up to ν_M is straightforward to calculate from Eq. (4).

The maximum spatial frequency that can be resolved, artifact free, at radius R is obtained by rewriting Eq. (4) as

$$\nu_M = \frac{M}{4\pi}\left(\frac{1}{R} - \frac{1}{\rho}\right). \tag{5}$$

Note that ν_M is proportional to the number of views and that as $R \to \rho$, $\nu_M \to 0$. It is a good rule of thumb not to image at radii greater than one-half of the fan source circle radius since artifacts are very likely to be present. Furthermore, as shown in Eq. (9), the noise increases significantly as the fan circle is approached.

III. Noise in the Reconstructed Image

The standard deviation of the reconstructed absorption at a point can be calculated from the statistics of the projection data noise for many scans. Let $e_j(n)$ denote the noise in the projections where j indices a fan source position and n indices the ray within the fan. If the correlation of the projections of different rays depends only on the angular separation of the rays within the fan and if the noise in the projections of one fan is uncorrelated with the noise in another fan, the expectation value of the noise correlation over an ensemble of measurements of the projections may be written as[30]

$$\langle e_j(n')e_{j'}(n'')\rangle = \sigma_p^2 f(|n' - n''|)\delta_{j,j'}, \tag{6}$$

where $f(t)$ gives the correlation spectrum of the projection noise normalized to the variance σ_p^2 of the projection noise, t is an index for the angle between rays in a fan, δ indicates a Kronecker delta function, and the symbol $\langle\ \rangle$ denotes expectation value. Equation (6) defines $f(t)$.

The reconstruction process convolves the projection data with a kernel function which determines the spatial

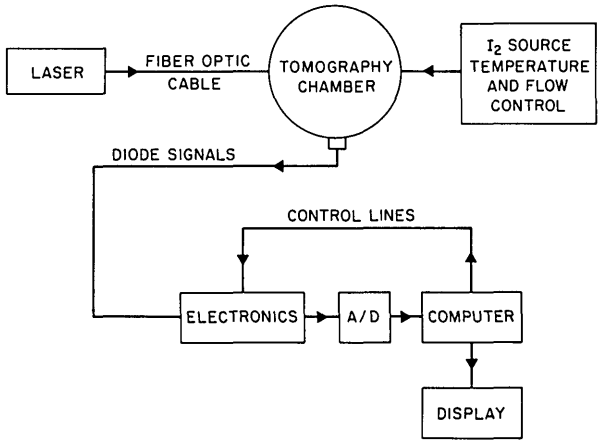

Fig. 4. Schematic diagram of tomography apparatus. Argon-ion laser light is guided by an optical fiber to the tomography chamber containing the iodine source and detectors. A computer controls the data acquisition electronics and reconstructs the image.

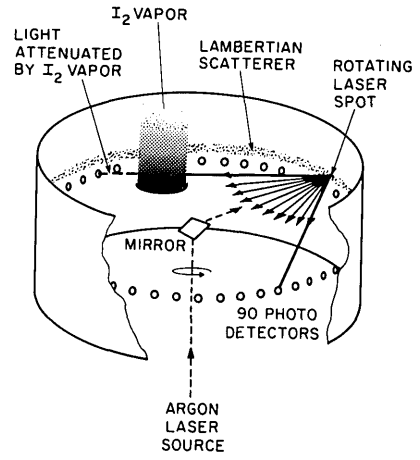

Fig. 5. Cutaway view of the fan beam geometry optical tomography chamber. The rotating mirror scans the laser spot around the Lambertian scattering screen. The screen and detectors are on the perimeter of a 28-cm radius circle. Iodine vapor absorbs light creating the test object.

resolution and spatial frequency response of the system. We have used our experimental results to investigate the benefits of degrading spatial resolution in order to reduce the noise. Reduction in the spatial resolution and noise is achieved by convolving the RL kernel with a triangle filter $s(n)$ of width d defined by

$$s(n) = \begin{cases} \dfrac{d - |n|}{d^2} & |n| \le d, \\ 0 & |n| > d \end{cases} \tag{7}$$

to generate a new kernel $\bar{k}(na)$ given by

$$\bar{k}(na) = \sum_{n'=-N}^{N} k(n'a)s(n - n'), \tag{8}$$

where the overbar indicates the smoothed kernel.

The smoothing function reduces the noise sensitivity at the cost of degrading the spatial resolution. Some care must be taken in choosing the smoothing filter to avoid misleading reconstructions.[30] The noise variance $\tilde{\sigma}^2(r)$ in the reconstructed image can be shown to be[30]

$$\tilde{\sigma}^2(r) = \frac{M}{\rho^2}\sigma_p^2 \frac{(1 + \frac{1}{2}r^2)}{(1 - r^2)^3} \sum_{t=0}^{N} f(t) \times \sum_{n=-\infty}^{\infty} R\{s\}(t - n)\bar{R}\{k\}(n), \quad [r < 1] \tag{9}$$

where M is the number of fan source positions on the full circle, and $r \equiv \tilde{r}/\rho$ is the distance of the reconstructed point from the center of the fan source circle normalized by the fan source circle radius. $\bar{R}\{k\}$ includes the effects of linear interpolation of the kernel given by

$$\bar{R}\{k\}(t) = \tfrac{2}{3}R\{k\}(t) + \tfrac{1}{6}R\{k\}(t - 1) + \tfrac{1}{6}R\{k\}(t + 1), \tag{10}$$

and $R\{\cdot\}$ denotes an operator for taking the autocorrelation of the function in the bracket. To evaluate Eq. (10) the autocorrelation of the kernel is needed. The autocorrelation of the RL kernel is[30]

$$R\{k\}(0) = \frac{\pi^2}{12M^2a^2},$$
$$R\{k\}(t) = \frac{(-1)^t}{2M^2t^2a^2}, \quad t = \pm 1, \pm 2, \ldots. \tag{11}$$

When Eq. (11) is inserted into Eqs. (9) and (10) and no smoothing filter is used, the noise power is seen to be inversely proportional to both the number of fans and the square of the spatial resolution. Unlike parallel beam geometry, noise in fan beam geometry reconstructions depends on the normalized distance r of the reconstructed point from the center of the fan source circle.

IV. Experimental Apparatus and Results

Figure 4 is a diagram of the tomography apparatus. The argon-ion laser light is directed by an optical fiber to the tomography chamber. The iodine source in the tomography chamber is temperature controlled. A PDP 11/44 computer controls the data acquisition electronics and calculates the reconstructions. A typical reconstruction takes 10 min to compute from data acquired in 100 msec.

The fan beam geometry optical tomography chamber is shown as a cutaway drawing in Fig. 5. A 6-mm diam rotating laser spot scattering off a Lambertian surface provides a diverging source of radiation to illuminate the fan. An encoder on the rotating mirror shaft measures the position of the laser spot. Rays diverge from the laser spot at the fan vertex to each of the 90 silicon photodiode detectors evenly spaced in a circle 10 mm below the rotating laser spot. The intensities of the rays are sampled after traversing the image field for each of the 90, 180, or 360 uniformly spaced fan source positions per mirror revolution. The data are averaged for 16 scans. Both the fan source and the detector circles are 28 cm in radius. Typical data acquisition time is limited by electronics to 100 msec/scan. However, it is readily possible to design for significantly shorter data

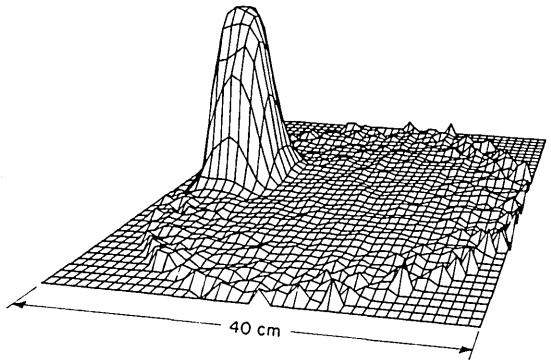

Fig. 6. Two-dimensional image of the 9.0-cm diam iodine vapor cloud at a vapor density of 0.6 Torr. The vertical scale is linear with a peak absorption of 0.036 cm^{-1} which is a factor of 125 greater than the statistical noise level of the reconstructed image. Ridges near the edge of the figure are reconstruction artifacts similar to those in Fig. 3.

acquisition times. The measurements are made using 2 W of multimode 514.5-nm argon-ion laser radiation. The optical path includes a multimodal optical fiber which guides the light from the argon-ion laser to the recollimating 25× microscope objective below the rotating mirror.

An iodine vapor plume was selected as the demonstration object because it absorbs argon-ion laser radiation, does not introduce Fresnel reflections or beam steering, and is relatively safe to handle. Iodine vapor is created by flowing nitrogen through a bed of iodine crystals placed in a 9-cm diam container with a temperature controlled outer jacket. The size of the iodine vapor plume is determined by placing an aperture over the source. Aperture sizes of 2.5 and 9.0 cm are used.

For absorption tomography a projection is the logarithm of the ratio of the transmitted intensity in the absence and presence of iodine vapor. The iodine-free transmission was determined from a normalization scan. The projections are corrected for background level and laser power fluctuations. For our virtual source geometry, the log of the radial absorption from the rotating mirror to the scatterer is subtracted to yield the projection values.

The laser power at the scatterer is not directly measured, so the absorption along the radial path is inferred from the apparent projections. Let A and B denote the ends of the line segment connecting the source and the detector passing through the mirror axis Z. The ray of a projection with source at A and detector at B double passes ZA and singly passes ZB. Similarly, the ray of a projection with source at B double passes ZB and singly passes ZA. These two simultaneous linear equations relating the absorption along ZAB and ZBA are solved to yield the radial absorption along ZA and ZB.

Figure 6 is an image of the iodine plume obtained at an iodine container temperature of 35°C corresponding to a saturated iodine vapor density of 800 ppm. The peak absorption level is 0.036 cm^{-1}, which is 125 times the noise level at the center of the reconstructed image. The noise has been reduced by convolving the RL kernel with a triangle smoothing filter [Eq. (7)] of width $d = 2$. The noise amplitude–absorption length product for a 2-cm pixel size is 6×10^{-4}, which is equivalent to an iodine concentration of 6 ppm. The noise in the averaged projections used to reconstruct the image is $\sim 10^{-2}$. The high sensitivity of tomography originates in the averaging effect of the views. A theoretical examination of the noise equivalent absorption $\delta_{\min}$ with spatial resolution of ρad is presented in a separate publication[30] and is shown to be approximated by

$$\delta_{\min} = \bar{\sigma}\rho ad \approx \sigma_p \sqrt{\frac{0.5}{Md}}, \qquad d > 1. \tag{12}$$

Note that the minimum detectable absorption is less than the noise in an individual ray of a projection by a factor of $\sqrt{0.5/Md}$, which is typically a reduction factor of 10–100.

The spatial resolution limits of our apparatus are verified by placing a 2.5-cm aperture on the source. A cross section of the iodine vapor vortex generated is the annular ring shown in Fig. 7(a). The reconstruction is performed using an unmodified RL kernel on a grid 11 cm across centered at $\bar{r} = 13.8$ cm. The spatial resolution is limited by the detector spacing.

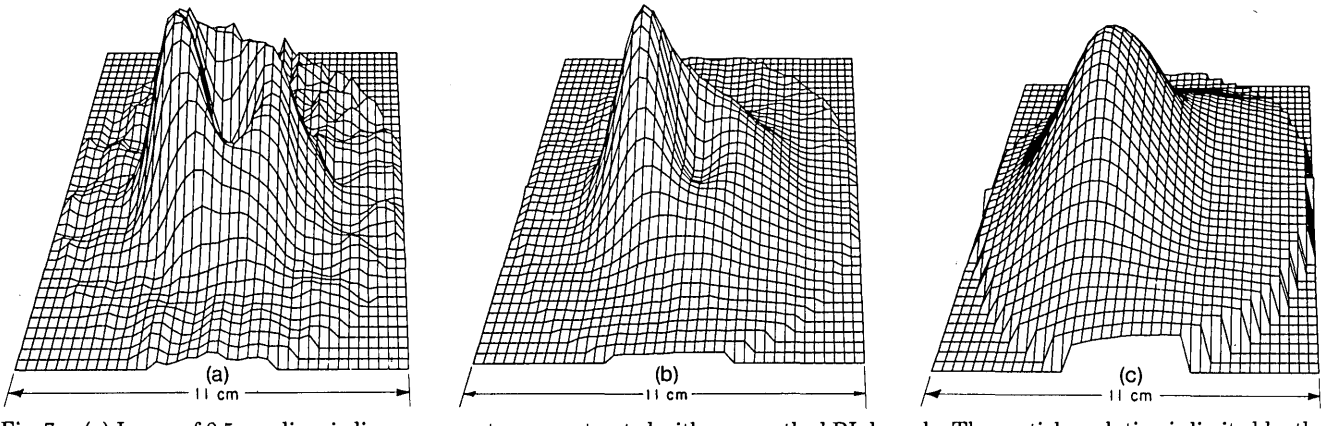

Fig. 7. (a) Image of 2.5-cm diam iodine vapor vortex reconstructed with unsmoothed RL kernel. The spatial resolution is limited by the detector spacing to ~1 cm. The reconstruction is centered 13.8 cm from the origin of the fan source circle. (b) Same as (a) but reconstructed with kernel convolved with a triangle filter of width $d = 2$ reducing the spatial resolution by a factor of 2. Note the loss of detail. (c) Same as (b) but with $d = 4$.

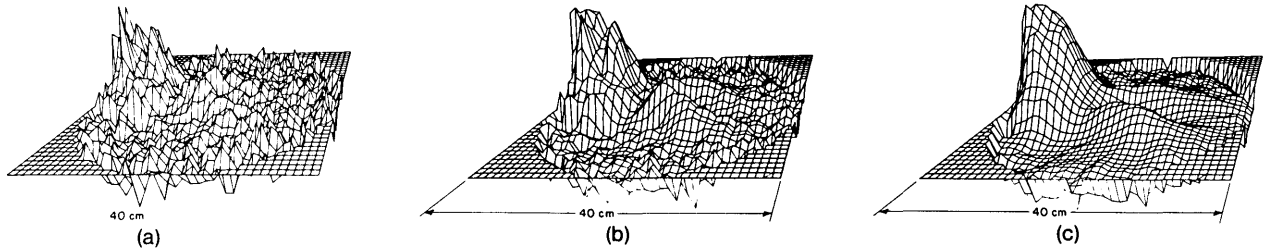

Fig. 8. (a) Image of low absorption iodine vapor cloud reconstructed with unmodified RL kernel. The iodine partial pressure is 0.06 Torr and the peak absorption coefficient is 0.007 cm^{-1}. (b) Same as (a) but reconstructed with RL kernel convolved with a triangle filter of width $d = 2$. (c) Same as (b) but with $d = 4$. Note the dramatic reduction in noise and reconstruction artifacts.

Convolving the RL kernel with triangle smoothing filters, Eq. (7), of widths $d = 2$ and $d = 4$ results in the images shown in Figs. 7(b) and (c), respectively. A filter of width $d = 2$ is sufficiently broad to eliminate most of the structure of the vortex indicating that the vortex structure is just resolvable.

The primary noise source in our experiment is laser speckle. The interference of coherent laser light scattered from the rough Lambertian scatterer gives rise to speckle at the detectors. Speckle is discussed by Francon[31] who shows that the grain size of speckle is inversely proportional to the size of the spot at the scatterer. Speckle is also introduced by the multimode optical fiber. Stressing the multimode fiber at frequencies above the detector bandwidth can reduce the speckle from coherent sources. The modulated speckle pattern can be averaged by the detector electronics. In addition, speckle from coherent sources is not a problem if only one optical path length exists from the source to the detector. This is the case when mirrors are used in place of the Lambertian scatterer and a single-mode optical fiber replaces the multimode fiber. Speckle is not a problem with incoherent light sources.

Figures 8(a)–(c) illustrate the improvement in image quality obtained by degrading spatial resolution. Figure 8(a) is an image of the iodine vapor obtained at a low iodine concentration corresponding to a temperature of 5°C, an equivalent vapor pressure of 0.06 Torr, and peak absorption of 0.007 cm^{-1}. An unmodified RL kernel is used for the reconstruction. The low ridges near the center of the image are due to iodine vapor created by sublimation of iodine from the mechanical supports. Figures 8(b) and (c) are reconstructed from the same data as Fig. 8(a) but with a kernel generated by convolving the RL kernel with triangle filters of widths $d = 2$ and $d = 4$, respectively.

Quantitative measurement of the mean image noise variance is a useful indicator of image quality. We experimentally investigate noise in our tomography system by constructing null tomograms in the absence of iodine. Figure 9 is a comparison of the measured noise amplitude in reconstructions using an unsmoothed RL kernel with the noise values predicted by Eqs. (9)–(11) using the actual correlations of the rays within the projections. The points in this figure represent twelve tomograms made in a wide variety of conditions including 90, 180, and 360 fan source positions per revolution. Agreement between the theoretical and experimental noise amplitude is excellent, having a standard deviation of 0.015.

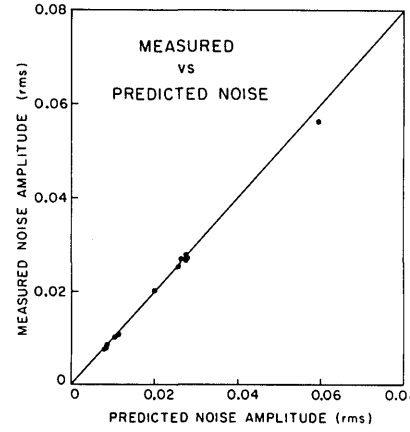

Fig. 9. Measured and predicted rms noise amplitudes for twelve independent null tomographic images. A null tomogram does not have the iodine absorber present and thus ideally has unity transmission across the image.

The dependence of the noise amplitude on the distance of the reconstructed point from the center of the fan source circle is a characteristic of fan beam geometry. The noise amplitude increases according to $G(r) = A(1 + \frac{1}{2}r^2)/(1 - r^2)^3$, where r is the distance of the reconstructed point from the center of the fan source normalized by the fan source circle radius, and the overall level A is determined by the amplitude and correlations of the projection noise. The solid line in Fig. 10 is a parameterless theoretical prediction of the noise amplitude vs distance from the center of the fan source circle of a reconstruction. The dots are the rms noise amplitude in annular rings of the reconstruction.

If the noise in the projections of different fans is uncorrelated, the image noise amplitude should be inversely proportional to the square root of the number of fan source positions on a full circle. Figure 11 is a graph of the noise amplitude vs the number of fan source positions. The lines represent a sequence of reconstructions obtained from different sets of data. In each sequence fans of projection data were omitted to generate data sets with fewer fans. The abbreviated

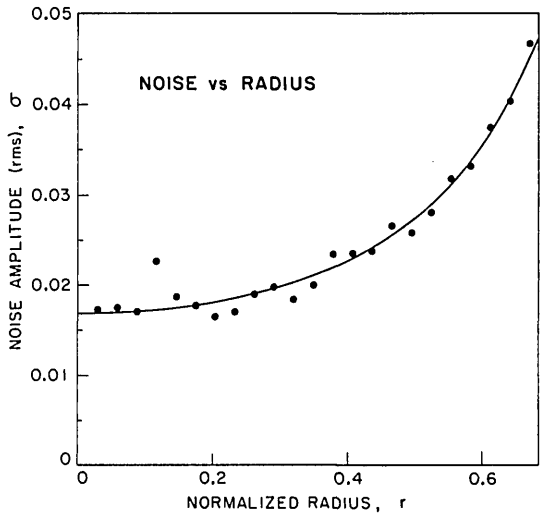

Fig. 10. Dependence of the rms noise amplitude in the reconstructed image on the normalized distance r of the point from the center of the fan source circle. The solid line is the parameterless prediction of Eq. (9), including the correlations of the projection data noise. The dots are measured noise amplitude values.

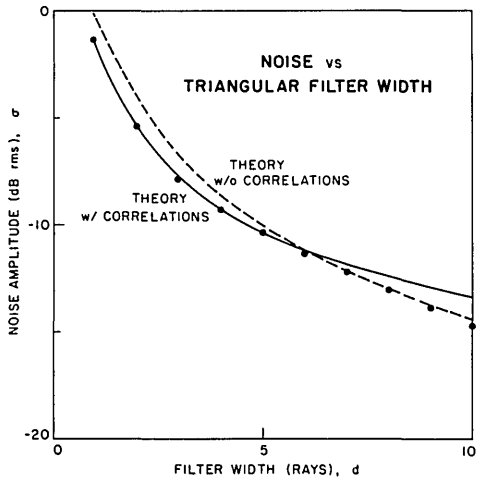

Fig. 12. Root-mean-square noise amplitude vs spatial resolution. The points are the rms noise in tomograms reconstructed using the RL kernel convolved with triangle filters of different widths d. The same projection data taken without iodine vapor present are used for all the reconstructions. The solid curve is the theoretical projection data. The dashed curve is the theoretical prediction of Eq. (9) assuming that the projection data are uncorrelated.

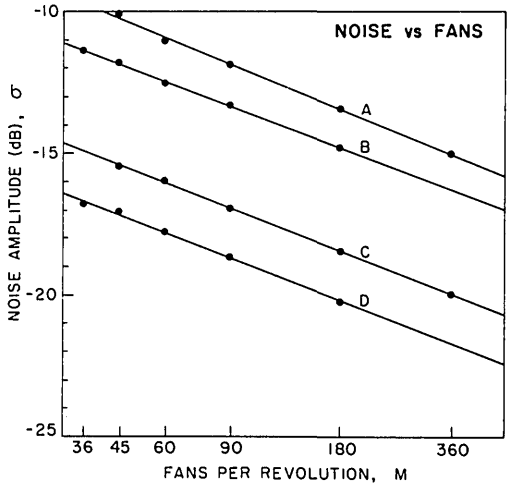

Fig. 11. Dependence of the rms noise amplitude on the number of fan source positions. The solid lines are least-squares fits to the measured points. The mean slope of the lines is 0.507 with a standard deviation of 0.016. The lines A–D correspond to different data sets with fans omitted to generate data sets with fewer fans.

data sets were used to reconstruct tomograms and the rms values of the noise inside a circle of normalized radius $r = 0.7$ are indicated by the dots. The lines are linear least-squares fit to the log–log data and have a mean slope of -0.507 with a standard deviation of 0.016. The theoretical value is -0.500 corresponding to the noise amplitude being inversely proportional to the square root of the number of fans.

The capability of reducing image noise by degrading the spatial resolution is illustrated in Fig. 12. The dots in Fig. 12 represent the rms noise amplitude in reconstructions obtained by convolving the RL kernel with triangle filters of Eq. (7) of various widths d. The convolution degrades the spatial resolution by approximately a factor of d. The reconstructions are all from the same projection data. Zero dB is defined as the noise in a reconstruction using an unmodified RL kernel with data which have the same variance as the actual data but are uncorrelated. The solid curve is a theoretical prediction including the measured correlations of the data. The dashed curve is the theoretical prediction assuming that the data are uncorrelated and is a useful assumption if the correlations within projections are unknown. Reducing the spatial resolution by a factor of 4, while holding constant the angular separation between detectors and the number of fan source positions, is adequate to obtain nearly a factor of 10 reduction in the noise.

V. Conclusions

In this paper we have studied noise, image quality, and detection sensitivity using optical tomography. Two sources of error exist in tomographic reconstructions. First, the finite sampling errors lead to aliasing and interpolation artifacts. Second, statistical noise is always present. In particular, speckle is a problem with coherent sources.

Experimental optical fan beam geometry tomography results verify a theoretical analysis of the effects of statistical noise on the reconstructed image including the dependence on the position of the reconstructed point in the image, the number of fan source positions per revolution M, the correlations and amplitude of the projection noise and the spatial resolution desired.

A theoretical analysis of the effects of these considerations is confirmed by a fan beam geometry optical tomography experiment imaging the iodine vapor density distribution in a plane. Extrapolated iodine concentration detectable in a 2-cm path length with a signal-to-noise ratio of unity is 6 ppm. The noise in our

tomographic images with 2-cm resolution corresponds to an absorption of 6×10^{-4} in a 2-cm path length and is nearly a factor of 20 less than the noise in individual projections showing that tomography is a sensitive image technique.

Tomography is a general technique for reconstructing the spatial distribution of any scalar variable for which a uniquely invertible function of the line integral of that variable can be obtained. The line integrals must form an intersecting mesh in the plane but need not satisfy the requirements of the fan beam or parallel beam geometries. Line integrals are available in measurements of the index of refraction either by interferometry[32] or from beam deflection measurements.[33,34] Other possible extensions include emission tomography and particulate distributions from scattering measurements. Three-dimensional information may be obtained by taking data in a sequence of stacked planes.

References

1. Special issue on Computerized Tomography, Proc. IEEE **71** (Mar. 1983).
2. A. M. Cormack, "Early 2-D Reconstruction (CT Scanning) and Recent Topics Stemming from It, Nobel Lecture 1979," J. Comput. Assist. Tomogr. **4,** 658 (1980).
3. G. N. Hounsfield, "Computed Medical Imaging, Nobel Lecture 1979," J. Comput. Assist. Tomogr. **4,** 665 (1980).
4. G. T. Herman, *Image Reconstruction from Projections: The Fundamentals of Computed Tomography* (Academic, New York, 1980).
5. H. H. Barrett and W. Swindell, *Radiological Imaging, Vols. 1 and 2* (Academic, New York, 1980).
6. R. N. Bracewell and A. C. Riddle, "Inversion of Fan Beam Scans in Radio Astronomy," Astrophys. J. **150,** 427 (1967).
7. G. T. Herman, A. V. Lakshminarayanan, and A. Naparstek, "Convolution Reconstruction Techniques for Divergent Beams," Comput. Biol. Med. **6,** 259 (1976).
8. R. L. Byer and L. A. Shepp, "Two-Dimensional Remote Air-Pollution Monitoring Via Tomography," Opt. Lett. **4,** 75, (1979).
9. M. J. Dyer and D. R. Crosley, "Two-Dimensional Imaging of OH Laser-Induced Fluorescence in a Flame," Opt. Lett. **7,** 382 (1982).
10. G. Kychakoff, R. D. Howe, and R. K. Hanson, "Quantitative Flow Visualization Technique for Measurements in Combustion Gases," Appl. Opt. **23,** 704 (1984).
11. J. C. McDaniel, D. Baganoff, and R. L. Byer, "Density Measurements in Compressible Flows Using Off-Resonant Laser Induced Fluorescence," Phys. Fluids **25,** 1105 (1982).
12. D. R. Crosley, "Collisional Effects on Laser Induced Fluorescence Flame Measurements," Opt. Eng. **20,** 511 (1981).
13. M. B. Long, D. C. Fourguette, M. C. Escoda, and C. B. Layne, "Instantaneous Ramanography of a Turbulent Diffusion Flame," Opt. Lett. **8,** 244 (1983).
14. E. Wolf, "Three Dimensional Structure Determination of Semi-Transparent Objects from Holographic Data," Opt. Commun. **1,** 153 (1969).
15. E. Wolf, "Determination of Scattered Fields by Holography," J. Opt. Soc. Am. **60,** 18 (1970).
16. M. V. Berry and D. F. Gibbs, "The Interpretation of Optical Projections," Proc. R. Soc. London Ser. **A314,** 143 (1970).
17. B. W. Stuck, "Estimating the Spatial Concentration of Certain Types of Air Pollutants," J. Opt. Soc. Am. **67,** 668 (1977).
18. D. C. Wolfe, Jr., and R. L. Byer, "Model Studies of Laser Absorption Computed Tomography for Remote Air Pollution Measurements," Appl. Opt. **21,** 1165 (1982).
19. K. R. Kirchartz, U. Muller, H. Oertel, Jr., and J. Zierep, "Axisymmetric and Non-Axisymmetric Convection in a Cylindrical Container," Acta Mech. **40,** 181 (1981).
20. I. Willms, "A Measurement Procedure for Acquisition of Spatial Inhomogeneous Aerosol Concentrations," Aerosols in Science, Medicine and Technology, 9 Conference 1981, Gesellschaft fur Aerosolforschung, Schmallenberg.
21. R. J. Santoro, H. G. Semerjian, P. J. Emmerman, and R. Goulard, "Optical Tomography for Flow Field Diagnostics," Int. J. Heat Mass Transfer **24,** 1139 (1981).
22. G. T. Herman and A. Naparstek, "Fast Image Reconstruction Based on a Radon Inversion for Applications for Rapidly Collected Data," SIAM (Soc. Ind. Appl. Math.) J. Appl. Math. **33,** 511 (1978).
23. G. N. Ramachandran and A. V. Lakshminarayanan, "Three Dimensional Reconstructions from Radiographs and Electron Micrographs: Application of Convolution Instead of Fourier Transforms," Proc. Natl. Acad. Sci. U.S.A. **68,** 2236 (1971).
24. L. A. Shepp and B. F. Logan, "The Fourier Reconstruction of a Head Section," IEEE Trans. Nucl. Sci. **NS-21,** 21 (1974).
25. D. A. Chesler and S. J. Riederer, "Ripple Suppression During Reconstruction in Transverse Tomography," Phys. Med. Biol. **20,** 632 (1975).
26. R. A. Brooks, G. H. Glover, A. J. Talbert, R. L. Eisner, and F. A. DiBianca, "A Source of Streaks in Computed Tomograms," J. Comput. Assist. Tomogr. **3,** 511 (1979).
27. Ref. 4, p. 163*ff.*
28. R. A. Brooks, G. H. Weiss, and A. J. Talbert, "A New Approach to Interpolation in Computed Tomography," J. Comput. Assist. Tomogr. **2,** 577 (1978).
29. P. M. Joseph and R. A. Schulz, "View Sampling Requirements in Fan Beam Computed Tomography," Med. Phys. **7,** 692 (1980).
30. K. Bennett and R. L. Byer, "Fan Beam Tomography Noise Theory," J. Opt. Soc. Am. A, submitted.
31. M. Francon, *Laser Speckle and Applications* (Academic, New York, 1979), Chap. 2.
32. H. Oertel, Jr., and K. Buhler, "A Special Differential Interferometer Used for Heat Convection Applications," Int. J. Heat Mass Transfer **21,** 1111 (1978).
33. O. Kafri, "Noncoherent Method for Mapping Phase Objects," Opt. Lett. **5,** 555 (1980).
34. E. Bar-Ziv, S. Sgulim, O. Kafri, and E. Keren, "Temperature Mapping in Flames by Moire Deflectometry," Appl. Opt. **22,** 698 (1983).

We gratefully acknowledge the support of the Air Force Office of Scientific Research, the Stanford University Energy Institution, and helpful discussions with Martin M. Fejer. The illustrations were drawn by Janet Okagaki.